Linear gyrokinetic simulation of high-*n* toroidal Alfvén eigenmodes in a burning plasma

Yang Chen,[1] Scott E. Parker,[1] J. Lang,[2] and G.-Y. Fu[2]
[1]*University of Colorado at Boulder, Boulder, Colorado 80309, USA*
[2]*Princeton Plasma Physics Laboratory, Princeton, New Jersey 08543-0451, USA*

(Received 28 June 2010; accepted 24 August 2010; published online 14 October 2010)

A hybrid gyrokinetic ions/massless fluid electron model is used to study the stability of high-*n* toroidal Alfvén eigenmodes (TAEs) in ITER [M. Shimada *et al.*, Nucl. Fusion **47**, S1 (2007)]. The hybrid model has been implemented in the particle-in-cell turbulence simulation code GEM [Y. Chen and S. E. Parker, J. Comput. Phys. **220**, 839 (2007)]. The adequacy of the hybrid model for simulating TAEs has been previously demonstrated [J. Lang *et al.*, Phys. Plasmas **16**, 102101 (2009)] by comparing the simulated TAE mode frequency and structure with an eigenmode analysis, and the thermal ion kinetic damping effect with analytic theory. By using a global particle-in-cell code the effects of large orbit width and nonlocal mode structures can be accurately included. Damping rate due to numerical filtering is carefully monitored, and convergence with respect to particle number, grid resolution, etc., is thoroughly tested. The simulations show that the most unstable modes in ITER lie in the rage of $10<n<20$. Thermal ion pressure effect and alpha particle nonperturbative effect are important in determining the mode radial location and stability threshold. The thermal ion Landau damping rate and radiative damping rate from the simulations are compared with analytical estimates. The thermal ion Landau damping is the dominant damping mechanism. Plasma elongation has a strong stabilizing effect on the alpha driven TAEs. The central alpha particle pressure threshold for the most unstable $n=15$ mode is about $\beta_\alpha(0)=0.7\%$ for the fully shaped ITER equilibrium. © *2010 American Institute of Physics*. [doi:10.1063/1.3490213]

I. INTRODUCTION

Numerical study of the energetic particle driven magnetohydrodynamic (MHD) instabilities is often based on the kinetic-MHD formalism,[1] in which the bulk plasma is modeled by the MHD equations and the energetic particles by drift or gyrokinetic equations. Background damping mechanisms due to the thermal species, such as Landau damping and radiative damping, are not included. Such damping mechanisms would have been included in simulations that solve the full gyrokinetic-Maxwell system of equations, as have been employed in the study of microturbulence and anomalous transport. However, direct application of gyrokinetic turbulence codes to global energetic particle driven modes is difficult, and has only been attempted recently using the GYGLES code[2,3] with a sophisticated control variate method and finite element representation of the fields. The difficulty arises from computational complexities peculiar to energetic particle driven, long wavelength modes, such as the toroidal Alfvén eigenmodes (TAEs). From a computational point of view, the energetic particle driven TAE problem differs from drift-wave turbulence primarily in two aspects. First, delicate wave-particle resonance plays a crucial role in cases of near marginal TAE instabilities typical of experimental situations, but is not considered to be important for drift waves. Second, particle-in-cell (PIC) turbulence simulation codes, such as GEM,[4] are developed under the assumption of conventional gyrokinetic ordering, in particular, the assumption that instabilities occur in the thermal ion-Larmor-radius range $k_\theta\rho_i\sim 1$. The algorithm uses conventional grid-based representation for the fields and requires fine spatial grids for low $k_\perp$ modes to accurately solve Ampere's equation,[5] hence is not efficient for long wavelength TAE modes with $k_\theta\rho_\alpha\sim 1$.

In this paper we use a hybrid gyrokinetic ions/massless fluid electron model to study the energetic particle driven TAE modes. Such a model has been implemented in GEM. The adequacy of the hybrid model for simulating TAEs was previously demonstrated by Lang *et al.*[6] and Nishimura,[7] by comparing the simulated TAE mode frequency and structure with an eigenmode analysis, and the thermal ion kinetic damping effect with an analytic theory. Here we apply the hybrid model to a linear calculation of the unstable eigenmodes for a plasma with parameter representative of ITER.[8] Such a linear calculation is best carried out with a linear eigenmode code, e.g., NOVA-K,[9] HINST,[10] PENN,[11] CASTOR-K,[12] or LIGKA,[13] since an eigenmode code not only gives the growth rates of unstable modes but also the total damping rates of stable modes, whereas an initial value code, such as GEM, can only compute the growth rates of unstable modes. All of these codes treat the energetic particles kinetically. NOVA-K and CASTOR-K are perturbative in that the eigenmode structure is calculated based on MHD equations and modification of the mode structure due to energetic particles is not considered. HINST, PENN, and LIGKA are nonperturbative; HINST is based on the high-*n* ballooning formalism which is rather involved for the analysis of global effects, and PENN uses a dielectric tensor model[14] for kinetic effects. Eigenmode analysis is often made with a number of simplifying assumptions, e.g., analytical zeroth-order particle trajectories. Energetic particles frequently have an orbit width

comparable to the device size, which not only makes it difficult to simplify the description of the trajectories but also makes the eigenmode problem essentially nonlocal in radius. The LIGKA code treats the finite orbit width effect fully numerically, with the integration along the equilibrium trajectories performed by the HAGIS code.[15] Thus for an unstable plasma a LIGKA calculation closely mimics a linearized δf PIC simulation, both integrating δf along the equilibrium trajectories. As a consequence of thus including the fully kinetic effects, an eigenmode code becomes computationally very demanding.[13] On the other hand, large orbit width effect and wave-particle resonance effect are readily included in a PIC simulation. By selectively including various terms in the model equations, various effects of interest, such as the effect of the scale length of the energetic particle distribution, finite Larmor radius (FLR) effects, and thermal ion pressure density effects, can be assessed.

The hybrid model as implemented in GEM is fairly complete in terms of the important physical effects that are included. The most important neglected effect appears to be the electron kinetic effects, including the trapped electron collisional damping of TAEs.[16] GEM's microturbulence model is of course fully kinetic with drift-kinetic electrons. However, the original GEM algorithm[4] was developed mainly for the study of microinstabilities on the thermal ion-Larmor gyroradius scale, $k_\perp \rho_i \sim 1$. It uses $p_\parallel = v_\parallel + eA_\parallel/m$, the canonical momentum of a particle in a perturbed magnetic field with vector potential $A_\parallel$, as a velocity coordinate, in order to eliminate the inductive component of the parallel electric field, $\partial A_\parallel/\partial t$, from the equations. However, doing so sets Ampere's equation in a very stiff form for tokamak plasmas, with the stiffness measure inversely proportional to $k_\perp^2$. While the validity of this algorithm for modes with $k_\perp \rho_i \sim 1$ has been proved by benchmarking, its applicability to energetic particle driven MHD-scale modes with $k_\perp \rho_\alpha \sim 1$ has not been exhaustively tested and verified. On the other hand, the hybrid model has been designed to reduce to the ideal MHD equations in the long wavelength limit, which makes a direct comparison with eigenmode analysis based on the ideal MHD equation possible and its validity for MHD modes readily established.[6] One is therefore motivated to account for the kinetic electron effect in an incremental manner, i.e., by using kinetic electron closure for the fluid equations. Such a closure scheme has been formulated and demonstrated for long wavelength Alfvén waves and short wavelength ion-temperature-gradient-driven (ITG) modes in a three-dimensional shearless slab. Details of the closure model and its implementation in GEM will be reported in the near future.

This paper is organized as follows. In Sec. II we present a few numerical details of the simulations. Section III presents results of linear simulations for model ITER parameters. Discussion and summary are presented in Sec. IV.

II. NUMERICAL METHODS

We refer the readers to Refs. 17 and 6 on details of the gyrokinetic ion/massless fluid electron hybrid model. Here we only briefly summarize the hybrid model for the sake of detailing the simulations. The perturbed electromagnetic field of the hybrid model is given by $\mathbf{B}_{\perp 1} = \nabla \times (A_\parallel \mathbf{b})$ and $\mathbf{E}_1 = -\nabla\phi - (\partial A_\parallel/\partial t)\mathbf{b}$, with $\mathbf{b}$ as the unit vector along the equilibrium magnetic field. The effect of nonzero $\delta B_\parallel$ is not considered in this paper. Given $\mathbf{E}_1$ and $\mathbf{B}_1$ the ion gyrokinetic equation is integrated in time to obtain the ion density n_{i1} and ion parallel flow $u_{\parallel i}$. The gyrokinetic Poisson equation is solved for the electric potential ϕ, and the parallel component of $\mathbf{E}_1 = -\nabla\phi - (\partial A_\parallel/\partial t)\mathbf{b}$ is cast into the form

$$\frac{\partial A_\parallel}{\partial t} = -\mathbf{b}\cdot\nabla\phi - E_\parallel, \tag{1}$$

which is integrated in time to obtain $A_\parallel$. Ampere's equation is then used to calculate the electron parallel flow $u_{\parallel e}$, which is needed to integrate the electron continuity equation to obtain the perturbed electron density n_{e1}. In this paper we only need the linearized electron continuity equation,

$$\frac{\partial \delta n_e}{\partial t} + n_0 B \nabla_\parallel \frac{u_{\parallel e}}{B} + \mathbf{v}_E \cdot \nabla n_0 + \frac{1}{m_e \Omega_e B^2}\mathbf{B}\times\nabla B\cdot\nabla(\delta p_{\perp e} + \delta p_{\parallel e}) + \frac{2n_0}{B^3}\mathbf{B}\times\nabla B\cdot\nabla\phi = 0. \tag{2}$$

The assumption of massless electrons is made in order to have a simplified Ohm's law for $E_\parallel$,

$$e n_0 E_\parallel = -\frac{\mathbf{B}_{\perp 1}}{B}\cdot\nabla p_{\parallel 0} - \mathbf{b}\nabla\,\delta p_{\parallel e}. \tag{3}$$

Here n_0 is the equilibrium electron density and $\delta p_{\parallel e}$ is the perturbed electron parallel pressure, which is approximately given by the electron's isothermal condition along the total magnetic field[18] in the massless fluid electron model. We note that the isothermal condition can be incorporated into Ohm's law, making numerically inverting the isothermal condition (a magnetic differential equation) unnecessary for solving Ohm's law.[17,19]

The last two terms on the left-hand side of Eq. (2) arise from the compressibility of the perturbed electron diamagnetic flow and the $E\times B$ flow, respectively. We have found that when thermal ions are included in the simulation the last term on the left-hand side must be included, otherwise the compressibility of ions' $E\times B$ motion, included in the ion gyrokinetic equation, will lead to unphysical charge separation. We will continue to drop the electron pressure term in Eq. (2) to avoid inverting the isothermal condition. In Sec. III we assess the effect of the δp_e term by assuming the electron temperature perturbation to be zero so that $\delta p_{\parallel e} = \delta p_{\perp e} = T_e \delta n_e$. The effect is found to be small. In any case, a satisfactory treatment of kinetic electron effect requires a kinetic electron extension to the fluid electron model. A scheme to close the pressure terms in the fluid electron equations with electron particles is discussed in Sec. IV.

A. Filtering and numerical dissipation

GEM uses the field-line-following coordinates (x,y,z) (Ref. 4), with x being the radial variable, y the field-line label within a flux-surface, and $z=q_0R_0\theta$ the coordinate along the field line. For linear single mode simulation the box length L_y is chosen such that the fundamental mode in y corresponds to the given toroidal mode number n. The electric potential ϕ is filtered along z after each Poisson solver by least-square fitting $\phi(x,k_y,z)$, with a set of piecewise quadratic blending functions,[20] which proceeds as follows. Define

$$N(s)=\begin{cases} s^2/2, & 0\le s\le 1 \\ -3/2+3s-s^2, & 1\le s\le 2 \\ (3-s)^2/2, & 2\le s\le 3 \\ 0, & \text{all else.} \end{cases} \tag{4}$$

The set of base functions defined on the N_z grid points along z is obtained from $N(s)$ through translation, taking into account the boundary condition each Fourier mode satisfies,

$$\begin{aligned}\Psi(m,x_i,k_y,z_k)=&N(kn_b/N_z-m)\\&+N(kn_b/N_z-m-n_b)p(x_i,k_y)\\&+N(kn_b/N_z-m+n_b)/p(x_i,k_y),\\&m=1,2,\ldots,n_b,\end{aligned} \tag{5}$$

where n_b is the number of base functions and $p(x_i,k_y)=\exp[-i2\pi r_0k_yq(x_i)/q_0]$ is a phase factor to ensure that Ψ for each m satisfy the toroidal boundary condition. A least-square fitting of $\phi(x_i,k_y,z_j)$ with this set of base functions is then performed.

It is also necessary to filter the electron parallel flow $u_{\parallel e}$, which is however best filtered with the digital filtering.[21] Digital filtering is also applied to $A_\parallel$ and δn_e. These two quantities are evolved in time, and applying the digital filtering to them each time step amounts to introducing a hyperviscosity term in the evolution equation, which incurs numerical damping of the modes. The amount of numerical dissipation is controlled with the parameter ϵ. If $A_\parallel^f$ is obtained by applying one pass of the digital filtering on $A_\parallel$, the new vector potential $A_\parallel'$ is calculated as

$$A_\parallel'=(1-\varepsilon)A_\parallel+\varepsilon A_\parallel^f. \tag{6}$$

The parameter ϵ should be chosen such that grid-scale instabilities are suppressed but the physical mode growth rate is not changed. We usually choose $\varepsilon<0.01$. Assuming $k_\parallel\sim 1/qR$ and $N_z=64$, the numerical damping rate caused by digital filtering is estimated to be

$$\gamma_{\text{num}}\Delta t=\tfrac{3}{16}\varepsilon(k_\parallel\triangle z)^4<1.7\times10^{-7}, \tag{7}$$

which is at least an order of magnitude smaller than the growth rates we observe in simulations.

B. δf method for the energetic particles with a slowing-down distribution

We assume the energetic particles to have a slowing-down distribution of the form

$$f_\alpha(\varepsilon,\mu,P_\zeta)=\frac{R(\langle\Psi\rangle)}{v^3+v_I^3} \tag{8}$$

where v_I is the crossover velocity at which the energetic particle slows down on the thermal ions as much as on the electrons and R models the radial profile of the energetic particles. Due to the large orbit width it is desirable to express this radial profile in terms of the average radial location $\langle\Psi\rangle$, the average of the poloidal magnetic flux. In the δf method the rate of change of $\langle\Psi\rangle$ in a perturbed wave field is needed in the particle weight equation. For passing particles we take $\langle\Psi\rangle\approx\Psi$. For trapped particles we make use of the fact that the toroidal canonical momentum $P_\zeta=m_\alpha v_\parallel/B-q_\alpha\Psi/R_0$ is a constant of motion and $\langle v_\parallel\rangle\approx0$, therefore

$$\langle\Psi\rangle\approx-\frac{R_0}{q_\alpha}P_\zeta. \tag{9}$$

The rate of change of $\langle\Psi\rangle$, $d\langle\Psi\rangle/dt$, can then be derived from the gyrokinetic equations of motion. The energetic particle weight evolution equation is then

$$\frac{dw}{dt}=\frac{1}{g}\frac{d\delta f_\alpha}{dt}. \tag{10}$$

The effect of the radial profile $R(\langle\Psi\rangle)$ enters the simulation not through loading but through the weight equation.

In the δf method loading the marker particles according to Eq. (8) is not necessary. It is much simpler to load particles according to the slowing-down distribution, but uniformly in space. That is, we load the energetic particles according to

$$g=\frac{1}{C_v}\frac{1}{v^3+v_I^3}, \tag{11}$$

with $C_v=(4\pi/3)\log(v_\alpha^3+v_I^3)/(v_{\min}^3+v_I^3)$ so that $\int g d\mathbf{x}d\mathbf{v}=V$, the simulated volume. The minimal velocity $v_{\min}$ is chosen to be about the bulk ion thermal speed.

The δf method is also used for the bulk ions. Due to their low kinetic energy, the bulk ions' equilibrium distribution is assumed to be a local Maxwellian in velocity, with radius dependent density and temperature profiles.

III. STABILITY OF HIGH-n TAEs IN ITER

We now use the hybrid model to study the linear stability of intermediate n TAEs in a plasma with the following parameters: $R_0=6$ m, $a=2$ m, $B_0=5$ T, $T_e(0)=T_i(0)=20$ KeV, and $n_e(0)=10^{20}/\text{m}^3$. The on-axis thermal plasma beta is then $\beta(0)=6.4\%$. The q-profile is $q(r)=1.2+2.7(r/a)^3$ and a parabolic profile is assumed for the thermal pressure, $P(r)=P(0)[1-(r/a)^2]$. The ion and electron temperatures are assumed to be equal, and the electron density profile is assumed to be flat. This set of parameters is intended as a nominal ITER discharge. The thermal ion temperature profile introduces r-dependence in the ion polarization density (in the quasineutrality condition) and the magnetic drift, as well as the effect of ion diamagnetic flow. All of these effects are self-consistently included in the gy-

rokinetic thermal ion model. The equilibrium flux-surface shape is specified with the Miller model.[22] Details of how general equilibrium configuration is implemented in GEM can be found in Ref. 4. In this paper for simplicity we neglect the contribution of plasma current to the equilibrium magnetic field strength, which is needed to calculate the magnetic drift motion.

The alpha particles are the only energetic particle species. The radial profile is

$$R(\langle\Psi\rangle) = \frac{3}{2\pi} n_e(0) \frac{T_i(0)}{E_\alpha} \frac{\beta_\alpha(0)}{\beta(0)} \left(\frac{P(r)}{P(0)}\right)^{7/2}, \tag{12}$$

where $E_\alpha = 3.5$ MeV is the alpha birth energy, $\beta_\alpha(0)$ is the core alpha particle beta, and $\beta(0) = 2\mu_0 P(0)/B^2$ is the core thermal beta. In Eq. (12) the radius r corresponds to the poloidal magnetic flux at the orbit-averaged value $\langle\Psi\rangle$. This distribution was used by Gorelenkov *et al.*[23] and was based on the assumptions that the fusion production rate is proportional to T^2 and the slowing-down time is proportional to $T^{3/2}$.

We carry out simulation with a single thermal ion species with $m_i/m_p = 2.5$ to mimic a 50-50 mix of D-T plasma. The simulation domain in radius is $0.1 < r/a < 0.9$. For each toroidal mode number the box size in the y-direction is chosen such that the fundamental mode in y corresponds to the toroidal mode number, $L_y = \pi a/nq_0$, with $q_0 = q(a/2)$. The simulation box size along the field line is $L_z = 2\pi q_0 R_0$.

A. Damping effect of thermal ions

We first assume circular, concentric magnetic equilibrium to facilitate the comparison between simulation results and analytical theory on mode frequencies and damping rates. For simplicity we also drop the ω_{*T} effect of the thermal ions by setting the ω_{*T} term in the ion weight equation to zero. The reason is that at the reference $\beta(0) = 6.4\%$ we find that the bulk plasma is unstable near the edge due to the thermal ion temperature gradient. The local ideal ballooning mode stability criterion for large-aspect-ratio, circular cross section plasma is given by[24]

$$-r\beta' < \left(\frac{2}{3}\hat{s}\right)^{1/2} \left(\frac{r}{Rq^2}\right). \tag{13}$$

According to this formula, the ITER equilibrium as specified above is unstable at $r/a > 0.63$ for $\beta(0) = 6.4\%$. Numerically we indeed find that the $n = 10$ mode is unstable without alpha particles, with the mode peaked near the edge, $r/a > 0.7$. The mode has a real frequency near the ion diamagnetic frequency $\omega_{*T} = nq_0|T'|/eBr$ evaluated at $r/a = 0.8$. The mode is stable at $\beta(0) = 5.6\%$, has a complex frequency of $\omega/\omega_{*T} = (1.6, 0.15)$ at $\beta(0) = 6.4\%$, and $\omega/\omega_{*T} = (1.67, 1.4)$ at $\beta(0) = 8\%$, with the growth rate increasing rapidly with β. In a real ITER discharge such localized edge mode is likely to be strongly affected by details of the edge pedestal, the study of which is beyond the scope of this paper. We therefore temporarily drop the ω_{*T} term in thermal ion gyrokinetic equation.

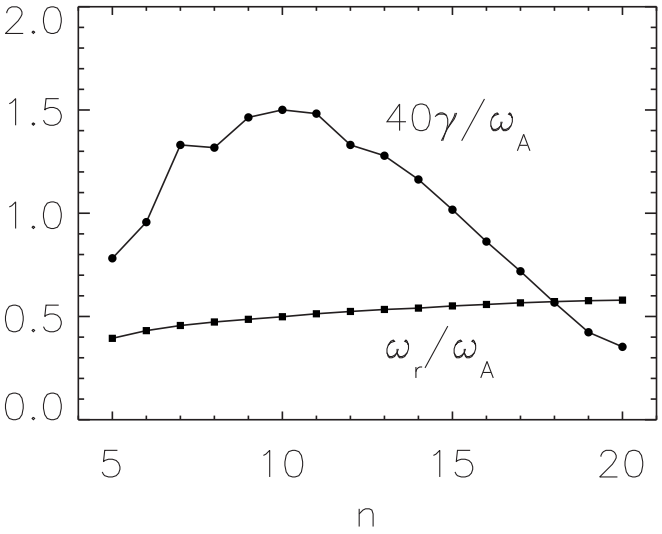

FIG. 1. Frequency and growth rate vs toroidal mode number n for circular concentric flux surfaces, $\beta_\alpha(0) = 1.8\%$.

Figure 1 shows the measured linear growth rates for toroidal mode numbers in the range of $4 < n < 21$, for $\beta_\alpha(0) = 1.8\%$. That the net growth rate peaks around $n \sim 10$ is consistent with previous analysis using the NOVA-K code.[23,25] The dependence of γ on the alpha particle beta for the $n = 10$ mode is shown in Fig. 2. The radial profiles of various poloidal harmonics of the electric potential ϕ for $\beta_\alpha(0) = 0.8\%$ and $\beta_\alpha(0) = 1.8\%$ are shown in Figs. 3 and 4, respectively. It is apparent that as $\beta_\alpha(0)$ increases from 0.8% to 1.8%, the mode peak radial location shifts outward, from $r/a < 0.6$ to $r/a > 0.6$. The $n = 10$ mode frequency also changes from $\omega/\omega_A = 0.55$ at $\beta_\alpha(0) = 0.8\%$ to $\omega/\omega_A = 0.5$ at $\beta_\alpha(0) = 1.8\%$. Here $\omega_A = v_A/q_0 R_0$ and $q_0 = q(r = a/2)$. Because of the simultaneous change in the mode structure and frequency, the mode growth rates do not depend on β_α strictly linearly, as would be expected from a perturbative analysis.

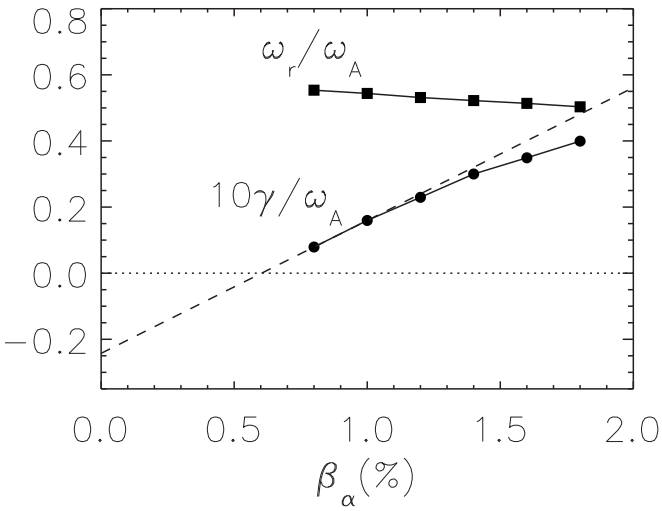

FIG. 2. Frequency and growth rate of the $n = 10$ mode vs $\beta_\alpha(0)$. Using the three lowest growth rate data to extrapolate to $\gamma = 0$ and $\beta_\alpha = 0$, one obtains a threshold $\beta_\alpha(0) \approx 0.6\%$ and thermal ion damping rate of $\gamma_d/\omega_A \approx 0.025$.

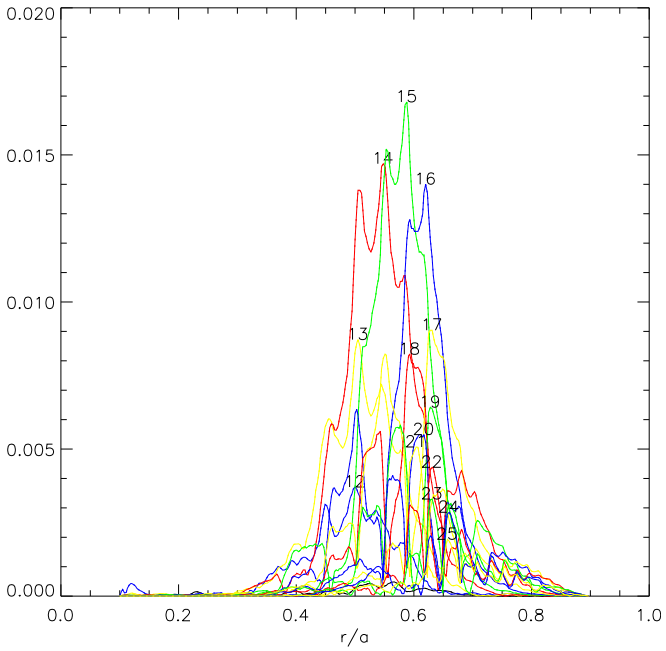

FIG. 3. (Color online) Radial profiles of poloidal harmonics $6 \le m \le 30$ for the electric potential, $n=10$, $\beta_\alpha(0)=0.8\%$.

If we fit the growth rates of the three lowest points linearly and extrapolate to the $\gamma=0$ line, we obtain an alpha particle threshold of $\beta_{\alpha c}(0)=0.6\%$ for the $n=10$ mode. The same linear extrapolation to $\beta_\alpha(0)=0$ yields a background damping rate of $\gamma_d/\omega_A \approx 2.5\%$, as can be seen in Fig. 2. However, the damping rate thus obtained cannot be straightforwardly identified with the background damping rate of the $n=10$ TAE in the absence of alpha particles because of the nonperturbative effect of alpha particles on the mode structure and frequency. In the fluid electron model used here the

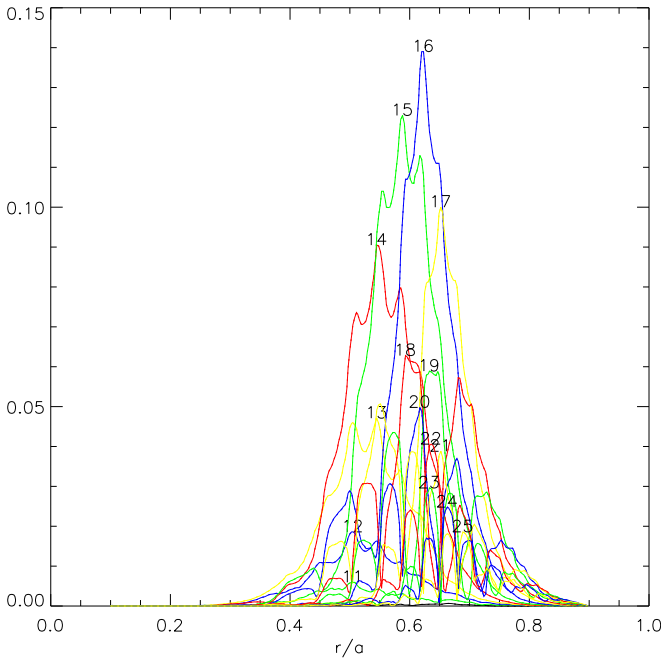

FIG. 4. (Color online) Radial profiles of poloidal harmonics $6 \le m \le 30$ for the electric potential, $n=10$, $\beta_\alpha(0)=1.8\%$.

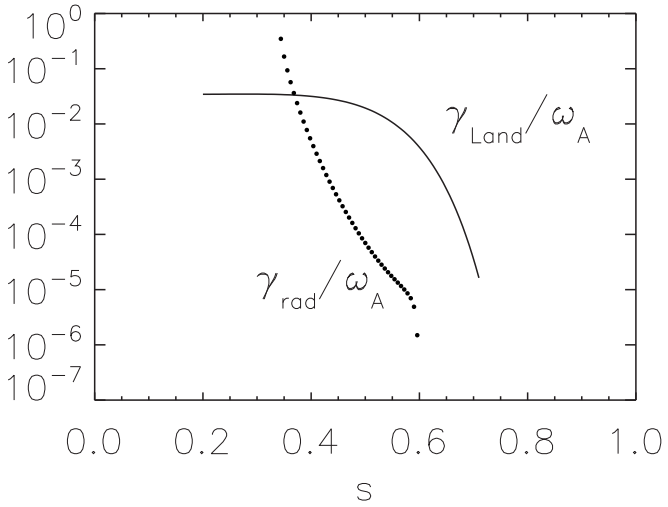

FIG. 5. Analytical estimates of thermal ion Landau damping (solid line) and radiative damping (dots) for $n=10$. The radiative damping is for a fixed mode frequency of $\omega/\omega_A(r/a=0.5)=0.523$.

electron collisional effects are neglected, and the background damping consists primarily of the thermal ion Landau damping and the radiative damping. Both damping mechanisms are sensitive to the actual mode location and frequency. In addition, the mode is also radially extended (as shown in Fig. 3), making it difficult to accurately estimate the damping rate. Here we use the analytical estimates of the radiative damping rate[9] and of the Landau damping rate[26] to shed some light on the simulation results, as obtained from extrapolation. For the radiative damping, assuming the mode is localized at the $q=q_m$ surface, where $q_m=(m+1/2)/n$, the radiative damping from the core thermal ions can be evaluated as

$$\frac{\gamma_{\rm rad}}{\omega_0}=\frac{1}{2}\hat{\epsilon}\frac{\omega^2}{\omega_0^2}\sqrt{(1-h_m)^3}\,\delta\alpha_m. \tag{14}$$

Here the effective aspect ratio is defined as $\hat{\epsilon}=2r_m/R_0$ in the absence of Shafronov shift, r_m is the mode radial location, $q_m=q(r_m)$, ω_0 is the ideal TAE mode frequency, and ω is the actual mode frequency. The quantities h_m and $\delta\alpha_m$ are defined in Ref. 9 and will be omitted here. In general, h_m and $\delta\alpha_m$ depend sensitively on the mode location and frequency. For the $n=10$ mode we fix the mode frequency at $\omega/\omega_A=0.523$ and calculate $\gamma_{\rm rad}$ as a function of radius for the ITER equilibrium q-profile as used in simulations. The result is plotted in Fig. 5 as the dotted line. The solid line is the estimated Landau damping rate using the formula of Fu and Cheng,[26]

$$\frac{\gamma_{\rm land}}{\omega}=-\sqrt{\pi}q^2\beta_i x_i^5 e^{-x_i^2}, \tag{15}$$

with $x_i=\omega/(k_\parallel 3\sqrt{2T_i/m_i})$, $k_\parallel=3/2qR$, and $\beta_i=2\mu_0 n_i T_i/B^2$ is the thermal ion beta. For the Landau damping estimate the same mode frequency $\omega/\omega_A=0.523$ is assumed. Equations (14) and (15) are local results that contain only local parameters; therefore it might not be accurate for a global mode. Nevertheless they contain essential physics and should be useful for understanding the simulation results. A third

damping mechanism, the continuum damping,[27,28] arises from coupling of TAE to the Alfvén continuum and is also self-consistently accounted for in the present hybrid model, but a simple formula for analytical estimate is not available.

The damping rate obtained from Fig. 2 corresponds to the damping rate of the mode at $\beta_\alpha(0)=0$. In order to compare this value with the analytical formulas, it is necessary to find the mode location at $\beta_\alpha(0)=0$. However, the precise mode location and frequency cannot be determined from the initial value calculations, which require an instability for a clear eigenmode to be observed. Generally speaking there are many damped eigenmodes in a global plasma. If the TAE eigenmode is the only weakly damped eigenmode, with all other eigenmodes rapidly decaying due to strong damping or phase-mixing, it is possible to obtain a clear TAE eigenmode starting from an initial state of a clearly formed eigenmode, for instance, the final state of a simulation with $\beta_\alpha(0)$ above the instability threshold. In practice, this turns out to be difficult. After hundreds of Alfvén wave periods no clear TAE eigenmode can be identified, indicating either that the TAE is not the least damped mode or the TAE damping rate is not well separated from the decaying rate of other modes. If the simulation is extended too long, the simulation ends in a state dominated by the noise of thermal ions. Due to this reason we resort again to an estimate of the mode location using extrapolation. The mode peak location at $\beta_\alpha(0)=0.8\%$ (Fig. 3) is taken to be $r/a=0.55$, while at $\beta_\alpha(0)=1.8\%$, it is taken to be at $r/a=0.65$; extrapolation to $\beta_\alpha=0$ gives a mode location of $r/a=0.47$. The mode frequency at $\beta_\alpha(0)=0$ can be similarly estimated to be $\omega/\omega_A\approx 0.6$. Using the mode location and frequency thus obtained in Eq. (15) yields a Landau damping rate of $\gamma_{\rm land}/\omega_A=1.5\%$, compared with the damping rate estimated from Fig. 2, $\gamma_{\rm land}/\omega_A=2.5\%$. The radiative damping rate as estimated from Eq. (14) depends on the mode location much more sensitively. For instance, at $r_m/a=0.38$ Eq. (14) gives $\gamma_{\rm rad}/\omega_A=1.6\%$, but a slight change in the mode location to $r_m/a=0.404$ leads to $\gamma_{\rm rad}/\omega_A=0.4\%$. In any case, at $r/a=0.47$ the radiative damping rate is negligible compared with the ion Landau damping rate.

We now use the $n=10$, $\beta_\alpha(0)=1.8\%$ case in Fig. 1 as a base case and test various effects by modifying the simulation and comparing with the result in Fig. 1. The radiative damping arises primarily from the thermal ion FLR effect in the polarization density in the gyrokinetic Poisson's equation.[6] The ion polarization density with FLR effect is

$$n_p=-\frac{qn_i}{T_i}\sum_{\mathbf{k}_\perp}\phi_{\mathbf{k}_\perp}e^{i\mathbf{k}_\perp\cdot\mathbf{r}}[1-\Gamma_0(b)], \tag{16}$$

with $b=k_\perp^2 v_{T_i}^2/\Omega_i^2$. In the long wavelength limit $b\to 0$ and $1-\Gamma_0(b)=b$, n_p becomes the MHD operator

$$n_p=\frac{m_i n_i}{qB^2}\nabla_\perp^2\phi. \tag{17}$$

If we replace n_p of Eq. (16) with n_p of Eq. (17), the $n=10$ mode frequency at $\beta_\alpha(0)=1.8\%$ changes from $\omega/\omega_A=(0.5,0.037)$ to $\omega/\omega_A=(0.5,0.039)$. The growth rate increases only slightly. Since the mode is located at $r/a>0.6$, the observed difference in the growth rates, attributable to radiative damping, is again consistent with the analytical estimate.

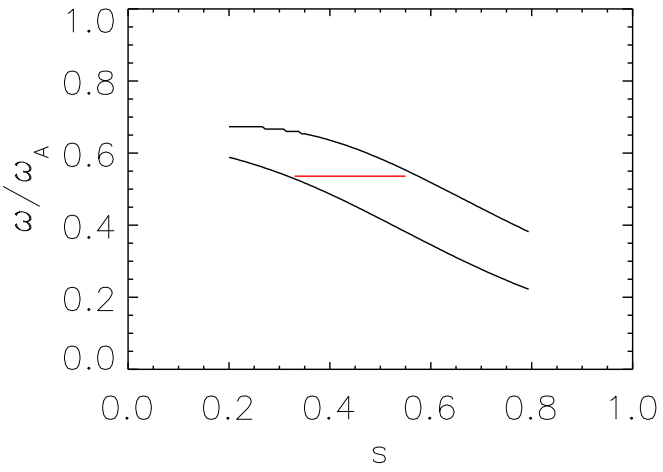

FIG. 6. (Color online) The $n=10$ mode frequency and location at $\beta_\alpha(0)=0$ with no thermal ions and using the MHD operator equation (17), compared with analytical estimates of the lower and upper bounds of the shear Alfvén continuum spectrum.

The thermal ion effect can be tested in the simulation by setting to zero the thermal ion contribution to the gyrokinetic Poisson equation and Ampere's equation, keeping only the polarization density. As remarked in Sec. II, this requires the $E\times B$ compressibility term in the electron continuity equation to be dropped as well, in order to avoid unphysical charge separation. Thus neglecting the thermal ion effect but still using Eq. (16) for the ion polarization term in the simulation, the $n=10$ mode frequency at $\beta_\alpha(0)=1.8\%$ becomes $\omega/\omega_A=(0.45,0.047)$. The decrease in the mode real frequency likely arises from a combination of the finite pressure modification of the continuum gap location[29] and possible change in the mode location. The increase in the growth rate, about $\Delta\gamma/\omega_A=1\%$, is again consistent with the large thermal ion Landau damping rate. However, because both the mode frequency and the mode structure change when the thermal ion response is set to zero, and the alpha particle drive likely changes as a consequence, the difference in the mode growth rate includes the effect of thermal ion Landau damping but is not identical with it.

To identify the unstable mode as TAE we have carried out simulations of the $n=10$ mode with the MHD operator equation (17) and without thermal ions. At $\beta_\alpha(0)=1.8\%$ the mode frequency is $\omega/\omega_A=(0.45,0.049)$. A scan over $\beta_\alpha(0)$ has been carried out in the unstable range and, extrapolating the results to $\beta_\alpha(0)=0$ as previously, we find the mode real frequency to be $\omega_r/\omega_A=0.53$ and location of the mode at $r/a\sim 0.45$. The lower and upper bounds of the shear Alfvén continuum spectrum at radius r for a high-n mode can be estimated using the analytic formula $\omega_\pm=(1\pm r/a)\times[v_A/2q(r)R_0]$. The results are plotted in Fig. 6. The mode frequency obtained from extrapolation is also indicated. It can be seen that the observed frequency lies within the continuum gap at the mode location, which proves that the unstable mode in the simulation is indeed a TAE.

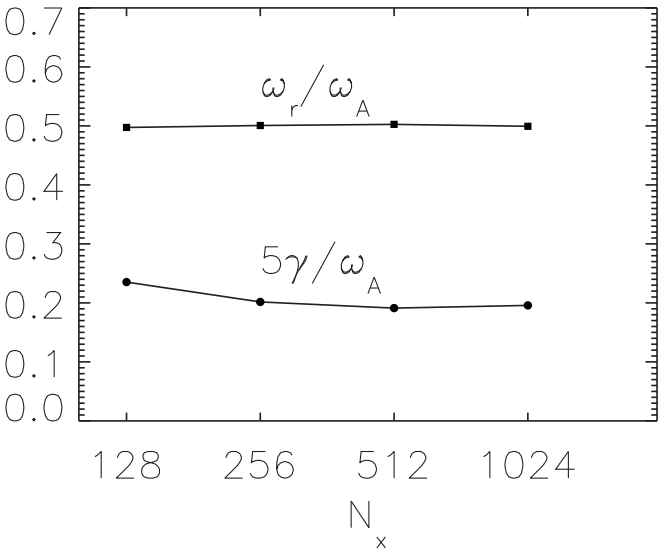

FIG. 7. Convergence test with respect to radial grid number.

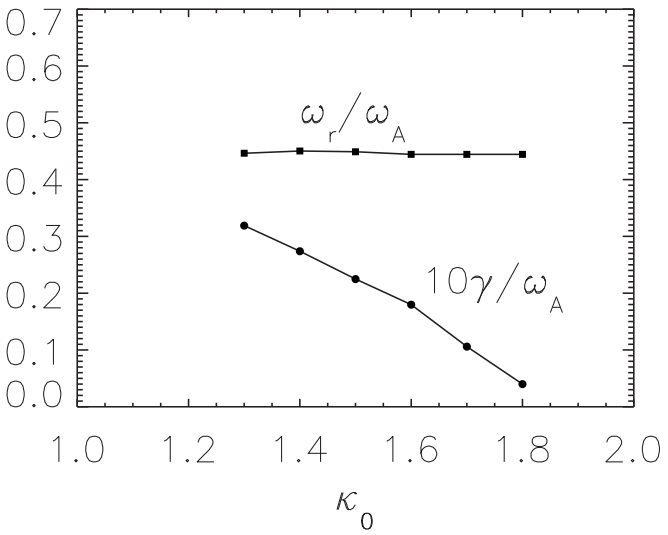

FIG. 8. $n=10$ mode frequency and growth rate vs elongation κ_0. Triangularity $\delta_0=0.5$ and Shafranov shift $R_0'=-0.16$ at the edge.

We can also test the effect of the electron diamagnetic term, the fourth term on the left-hand side of Eq. (2), by assuming $\delta p_{\parallel e}=\delta p_{\perp e}=T_e\delta n_e$, i.e., assuming electron temperature perturbations to be zero both parallel and perpendicular to the magnetic field. This leads to a mode frequency of $\omega/\omega_A=(0.52,0.038)$, a rather small change in the growth rate. However, as remarked in Sec. II, fully kinetic electron effect such as electron collisional damping can only be accurately included in the fluid model using a kinetic electron closure, which is beyond the scope of this paper.

The simulation results are converged with respect to particle numbers. We normally use 1 048 576 particles per species for these single mode simulations. Doubling the particle number leads to no observable change in the mode frequency and growth rate. The number of grids used to obtain Figs. 1 and 2 are $(N_x,N_y,N_z)=(512,32,64)$ and the time step is $\omega_A\Delta t=0.007\,65$. This time step is chosen primarily to avoid numerical instabilities, but reducing the time step by half leads to the same mode frequency and growth rate for the above $n=10$ mode test case. Of most concern in such convergence study is the grid number in the radial direction because of the possible fine radial structures arising from excitation of kinetic Alfvén waves. Figure 7 shows the results of simulations of the test case with difference N_x. While $N_x=128$ leads to a significantly larger growth rate, the $N_x=512$ result is well converged.

B. Stability with shaped flux surfaces

We now turn to stability of shaped plasmas. GEM uses the Miller formula for the flux-surface shape,

$$R=R_0(r)+r\cos[\theta+\arcsin\,\delta(r)\sin\,\theta],$$
$$Z=\kappa(r)r\sin\,\theta, \tag{18}$$

which models a shaped equilibrium with a Shafranov profile $R_0(r)$, elongation profile $\kappa(r)$, and triangularity profile $\delta(r)$. The Shafranov shift is specified according to

$$R_0(r)=R_0(a)-\frac{aR_0'}{2}\left[1-\left(\frac{r}{a}\right)^2\right], \tag{19}$$

where R_0' is a constant. The triangularity profile is

$$\delta(r)=\delta_0\left(\frac{r}{a}\right)^2 \tag{20}$$

and the elongation profile is

$$\kappa(r)=\kappa_0-0.3+0.3\left(\frac{r}{a}\right)^4. \tag{21}$$

The nominal ITER parameters are $\kappa_0=1.8$, $\delta_0=0.5$, and $R_0'=-0.16$.

We first continue to drop the ion ω_{*T} effect, and examine the effect of elongation on the $n=10$ mode, at fixed $\beta_\alpha(0)=1.8\%$, $\delta_0=0.5$, and $R_0'=-0.16$. The result is shown in Fig. 8. The $n=10$ mode is nearly stable with the full ITER shape parameters. We believe that the reduction of mode growth rates due to elongation is mainly the result of reduced alpha particle drive. Since the alpha density profile is fixed in r, which is the flux-surface radius at the middle plane, elongation in effect increases the average radius and reduces the average spatial radial gradient of the alpha particle distribution. The mode poloidal structures for ϕ and $A_\parallel$ at $\kappa_0=1.7$ are shown in Figs. 9 and 10, respectively. The mode frequencies for toroidal mode number in the range $8<n<26$ for $\beta_\alpha(0)=3\%$ at the nominal ITER shape parameters are shown in Fig. 11, which indicates that the most unstable mode is $n=15$. The results of $\beta_\alpha(0)$ scan for $n=15$, similar to those used to obtain Fig. 2, are plotted in Fig. 12. Using a linear fit we obtain an instability threshold for the $n=15$ mode, $\beta_{\alpha c}=1.1\%$.

Finally we turn on the thermal ion temperature gradient effect. For the parabolic thermal pressure profile the quantity $\kappa_T\rho_i=\rho_i|d\ln P(r)/dr|$ increases monotonically with r and is about 0.01 at $r_{\rm out}=0.9a$, the simulation boundary. As remarked above, stability at such edge locations is likely to be affected by the edge pedestal. For our purpose it is desirable

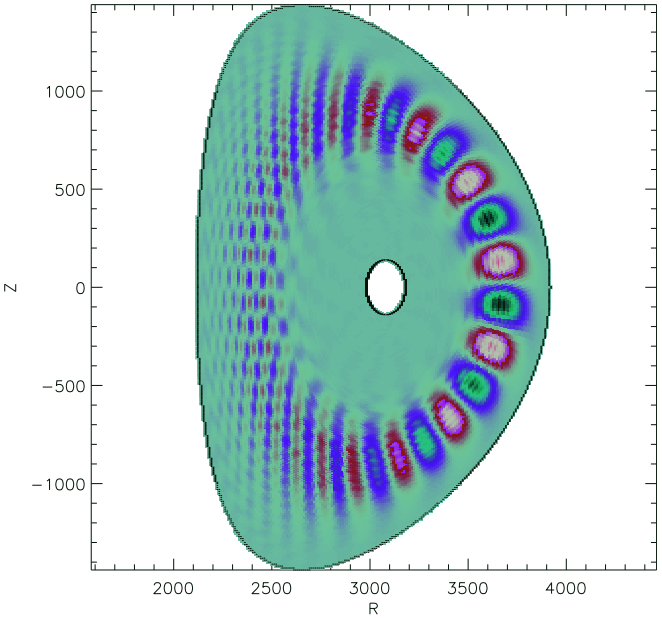

FIG. 9. (Color online) $n=10$ mode poloidal contour plot for ϕ with $\kappa_0=1.7$.

to remove any edge effect on the core TAE modes. This can be done by multiplying $\kappa_T(r)$ by a factor of $(1-\exp[(r-r_{\text{out}})^2/(\Delta r)^2])$ so that κ_T is reduced within a radial slice of width Δr near the boundary, but unchanged elsewhere. We use $\Delta r=0.05a$ in the following simulations. The $n=10$ ballooning mode simulations mentioned above are also done with this modification of κ_T profile. With the specified shape profiles the $n=15$ ballooning mode is actually stable. The TAE mode frequencies for toroidal mode number in the range $8<n<26$ for $\beta_\alpha(0)=3\%$ at the nominal ITER shape parameters are shown in Fig. 13. Similar to the $\kappa_T=0$ results of Fig. 11, the most unstable mode is still $n=15$. The thermal ion temperature gradient decreases the mode frequencies, by

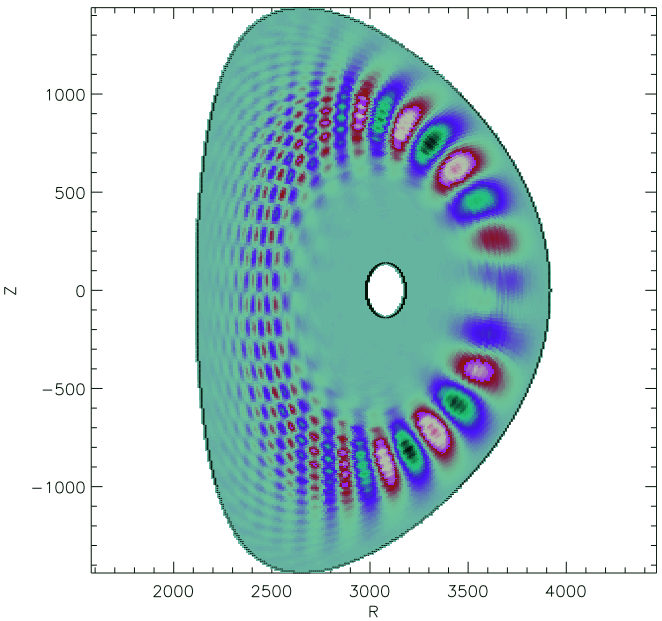

FIG. 10. (Color online) $n=10$ mode poloidal contour plot for $A_\parallel$ with $\kappa_0=1.7$.

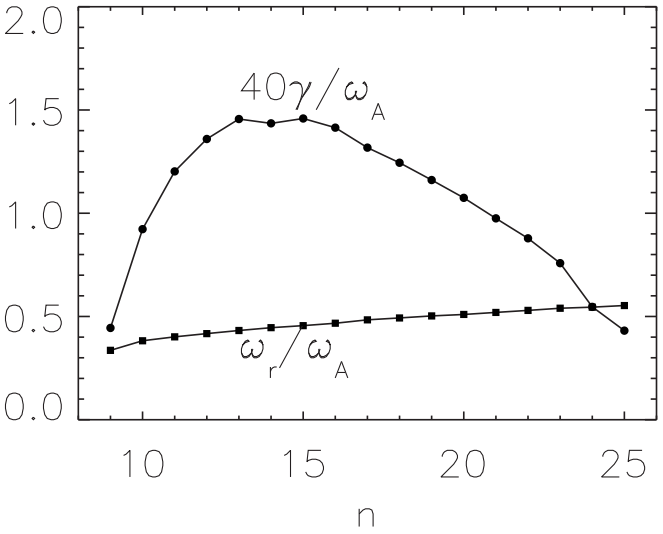

FIG. 11. Frequency and growth rate vs toroidal mode number n for shaped flux surfaces, $\kappa_T=0$, $\beta_\alpha(0)=3\%$.

about 10% for the $n=15$ mode, and increases the mode growth rates, nearly by 50% for $n=15$. By scanning over β_α (Fig. 14) we found that the effect of ∇T_i enhances the TAE growth rate for $n=15$ at all $\beta_\alpha(0)$. This is not always the case, however, for instance, in circular plasma simulations of the $n=10$ mode we found that at lower plasma β the ion temperature gradient actually reduces the TAE growth rates. The enhancement of the growth rate of the $n=15$ mode due to ∇T_i effect does not have a simple explanation. Both global effects and the strong flux-surface shaping make theoretical analysis difficult. It appears that the increase in the growth rate of the $n=15$ mode cannot be attributed to the change in the Landau damping rate as a result of the changes in the mode frequency and location. The location of the mode is not significantly shifted due to ∇T_i. The analytical formula (15) predicts that the Landau damping rate is $\gamma_{\text{land}}/\omega_A=0.6\%$ using the mode frequency and location with ∇T_i effect, compared with the estimated value of $\gamma_{\text{land}}/\omega_A$

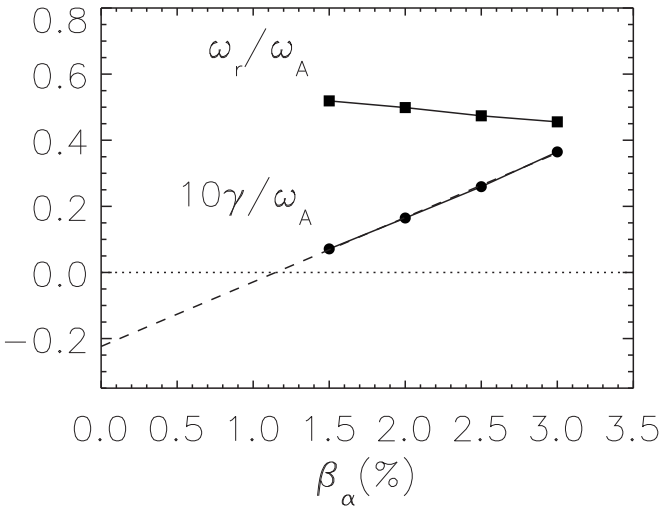

FIG. 12. Frequency and growth rate of the $n=15$ mode vs $\beta_\alpha(0)$, shaped plasmas, $\kappa_T=0$.

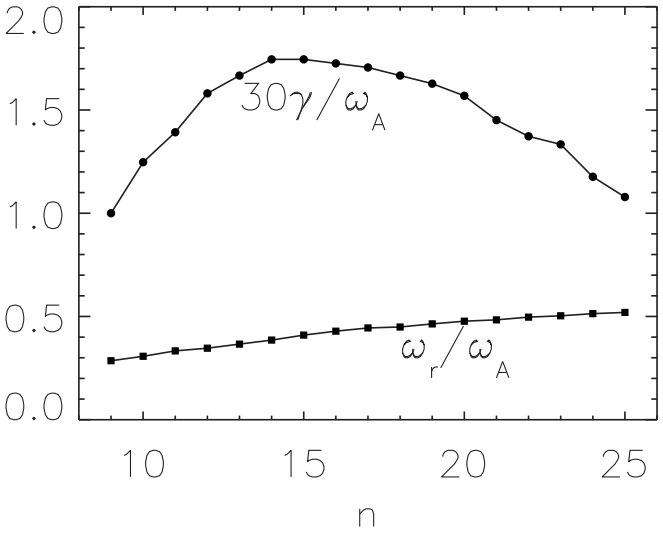

FIG. 13. Frequency and growth rate vs toroidal mode number n for shaped flux surfaces, $\kappa_T \neq 0$, $\beta_\alpha(0)=3\%$.

$=0.85\%$ using the mode frequency and location without the ∇T_i effect. On the other hand, the relatively large effect of ion temperature gradient on the mode growth rate is consistent with the large Landau damping rate, as estimated from the analytical expression (15). Due to the relatively high-β of the ITER equilibrium used here, the resonance speed of $v_A/3$ is only about three times the ion thermal speed near $r/a=0.5$, and thermal ion kinetic effects, both as an Alfvén instability drive[30,31] and a damping mechanism, can be significant.

The stability threshold of $n=15$ is also changed by ion temperature gradient effects, as shown in Fig. 14, which shows the threshold $\beta_\alpha(0)\sim 0.7\%$ and a background thermal ion damping rate of $\gamma_d/\omega_A \sim 2\%$, similar to the $\kappa_T=0$ results of Fig. 12.

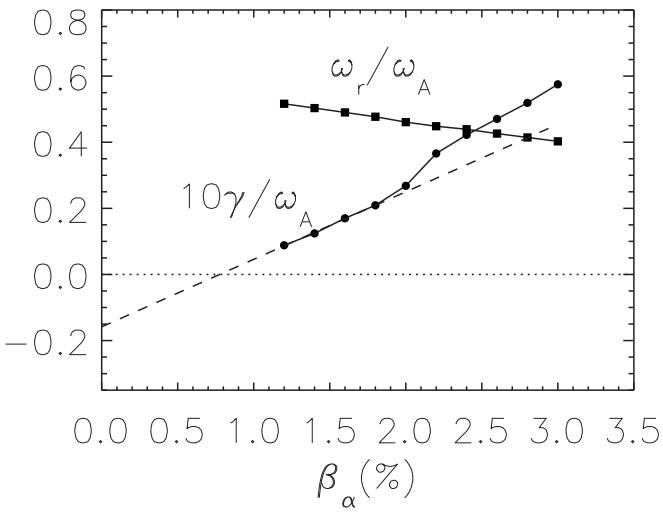

FIG. 14. Frequency and growth rate of the $n=15$ mode vs $\beta_\alpha(0)$, shaped plasmas, $\kappa_T \neq 0$.

IV. SUMMARY

We have carried out linear simulations of high-n TAEs in ITER-like plasmas using a hybrid gyrokinetic ion/fluid electron model. The simulations include alpha particles as the only energetic particle species. The simulations confirm that the most unstable modes in ITER lie in the rage of $10<n<20$, or $k_\theta \rho_\alpha \sim 1$. With nonperturbative thermal ions and alpha particles, the most unstable modes are located near $r/a \geq 0.5$ with a broad radial profile. The dominant background damping mechanism is the thermal ion Landau damping. Plasma elongation was shown to have a strong stabilizing effect on the alpha driven TAEs. The threshold for instability is about $\beta_\alpha(0)=0.7\%$ for the fully shaped ITER equilibrium.

The present numerical study of TAE instability in ITER is novel in a number of aspects. The hybrid model includes a fully kinetic treatment of the thermal ions, which, together with a nonperturbative approach, accounts for both the ion Landau damping and the radiative damping effects. The simulations are radially global, therefore accounts for two–dimensional (2D) effects that are difficult to analyze in a high-n ballooning analysis. By using a particle-in-cell approach, the large orbit width effect of energetic particles is computed accurately. The orbit width effect is particularly difficult for a direct eigenmode approach such as LIGKA, which computes the distribution function by integrating δf along the unperturbed trajectories. There are two main limitations on the present approach. The first is that these simulations are initial value calculations and require a sufficiently large net linear growth rate so that a clear eigenmode can emerge from numerical noise in a reasonable time. This means that the instability threshold must be estimated indirectly, i.e., by extrapolating from simulation results above the threshold. The second limitation is the omission of electron damping effect due to the use of a collisionless fluid electron model. We have formulated a kinetic closure scheme for the present fluid electron model. This amounts to calculating the pressure terms in the electron continuity equation and Ohm's law for $E_\parallel$ using the drift-kinetic equation. Ohm's law must be modified to include the finite electron mass effect, as well as the ion terms if ion acoustic waves (IAWs) are to be included.[32] These terms are neglected in the simplified Ohm's equation, Eq. (3), but IAW is included in the massless electron fluid model via the further assumption of isothermal electron temperature. The implementation of the closure scheme in the GEM code and TAE simulations with kinetic electron effects will be reported in the future.

ACKNOWLEDGMENTS

This work was supported by the United States Department of Energy Plasma Energetic Particle Simulation Center. The simulations are carried out on the CRAY XT4 massively parallel process system at the National Energy Research Scientific Computing Center.

[1] W. Park, S. Parker, H. Biglari, M. Chance, L. Chen, C. Z. Cheng, T. S. Hahm, W. W. Lee, R. Kulsrud, D. Monticello, L. Sugiyama, and R. White, Phys. Fluids B **4**, 2033 (1992).
[2] A. Mishchenko, A. Konies, and R. Hatzky, Phys. Plasmas **16**, 082105 (2009).

[3]R. Hatzky, A. Konies, and A. Mishchenko, J. Comput. Phys. **225**, 568 (2007).
[4]Y. Chen and S. E. Parker, J. Comput. Phys. **220**, 839 (2007).
[5]Y. Chen and S. E. Parker, J. Comput. Phys. **189**, 463 (2003).
[6]J. Lang, Y. Chen, S. E. Parker, and G.-Y. Fu, Phys. Plasmas **16**, 102101 (2009).
[7]Y. Nishimura, Phys. Plasmas **16**, 030702 (2009).
[8]M. Shimada, D. J. Campbell, V. Mukhovatov, M. Fujiwara, N. Kirneva, K. Lackner, M. Nagami, V. D. Pustovitov, N. Uckan, J. Wesley, N. Asakura, A. E. Costley, A. J. H. Donne, E. J. Doyle, A. Fasoli, C. Gormezano, Y. Gribov, O. Gruber, T. C. Hender, W. Houlberg, S. Ide, Y. Kamada, A. Leonard, B. Lipshultz, A. Loarte, K. Miyamoto, V. Mukhovatov, T. H. Osborne, A. Polevoi, and A. C. C. Sips, Nucl. Fusion **47**, S1 (2007).
[9]G. Y. Fu, C. Z. Cheng, R. Budny, Z. Chang, D. Darrow, E. Fredrickson, E. Mazzucato, R. Nazikian, K. Wong, and S. Zweben, Phys. Plasmas **3**, 4036 (1996).
[10]N. Gorelenkov, C. Z. Cheng, and W. M. Tang, Phys. Plasmas **5**, 3389 (1998).
[11]A. Jaun, K. Appert, J. Vaclavik, and L. Villard, Comput. Phys. Commun. **92**, 153 (1995).
[12]D. Borba, H. L. Berk, B. N. Breizman, A. Fasoli, F. Nabais, S. D. Pinches, S. E. Sharapov, D. Testa, and contributors to the EFDA-JET Workprogramme, Nucl. Fusion **42**, 1029 (2002).
[13]P. Lauber, S. Gunter, A. Konies, and S. D. Pinches, J. Comput. Phys. **226**, 447 (2007).
[14]S. Brunner and J. Vaclavik, Phys. Fluids B **5**, 1695 (1993).
[15]S. D. Pinches, L. Appel, J. Candy, S. Sharapov, H. Berk, D. Borba, B. Breizman, T. Hender, K. Hopcraft, G. Huysmans, and D. W. Kerner, Comput. Phys. Commun. **111**, 133 (1998).
[16]N. N. Gorelenkov and S. E. Sharapov, Phys. Scr. **45**, 163 (1992).
[17]Y. Chen and S. E. Parker, Phys. Plasmas **8**, 441 (2001).
[18]P. Snyder and G. Hammet, Phys. Plasmas **8**, 744 (2001).
[19]B. I. Cohen, A. M. Dimits, W. Nevins, Y. Chen, and S. E. Parker, Phys. Plasmas **9**, 251 (2002).
[20]J. Candy and R. Waltz, J. Comput. Phys. **186**, 545 (2003).
[21]C. Birdsall and A. Longdon, *Plasma Physics via Computer Simulation* (McGraw-Hill, New York, 1985).
[22]R. L. Miller, M. S. Chu, J. M. Greene, Y. R. Lin-Liu, and R. E. Waltz, Phys. Plasmas **5**, 973 (1998).
[23]N. Gorelenkov, H. L. Berk, R. Budny, C. Z. Cheng, G.-Y. Fu, W. W. Heidbrink, G. J. Kramer, D. Meade, and R. Nazikian, Nucl. Fusion **43**, 594 (2003).
[24]J. Freidberg, Rev. Mod. Phys. **54**, 801 (1982).
[25]N. Gorelenkov, H. L. Berk, and R. Budny, Nucl. Fusion **45**, 226 (2005).
[26]G. Y. Fu and C. Z. Cheng, Phys. Fluids B **4**, 3722 (1992).
[27]F. Zonca and L. Chen, Phys. Rev. Lett. **68**, 592 (1992).
[28]M. N. Rosenbluth, H. L. Berk, J. W. Van Dam, and D. M. Lindberg, Phys. Rev. Lett. **68**, 596 (1992).
[29]C. Z. Cheng and M. S. Chance, Phys. Fluids **29**, 3695 (1986).
[30]R. Nazikian, H. L. Berk, R. V. Budny, K. H. Burrel, E. J. Doyle, R. J. Fonck, N. N. Gorelenkov, C. Holcomb, G. J. Kramer, R. J. Jayakumar, R. J. La Haye, G. R. McKee, M. A. Makowski, W. A. Peebles, T. L. Rhodes, W. M. Solomon, E. J. Strait, M. A. VanZeeland, and L. Zeng, Phys. Rev. Lett. **96**, 105006 (2006).
[31]F. Zonca, L. Chen, and R. A. Santoro, Plasma Phys. Controlled Fusion **38**, 2011 (1996).
[32]Y. Chen and S. E. Parker, Phys. Plasmas **16**, 052305 (2009).